Two zinc-binding domains in the transporter AdcA from *Streptococcus pyogenes* facilitate high-affinity binding and fast transport of zinc

Received for publication, September 21, 2017, and in revised form, February 25, 2018 Published, Papers in Press, February 28, 2018, DOI 10.1074/jbc.M117.818997

Kun Cao[1], Nan Li[1], Hongcui Wang[1], Xin Cao, Jiaojiao He, Bing Zhang, Qing-Yu He[2], Gong Zhang[3], and Xuesong Sun[4]

From the Key Laboratory of Functional Protein Research of Guangdong Higher Education Institutes, Institute of Life and Health Engineering, College of Life Science and Technology, Jinan University, 601 Huang-Pu Avenue West, Guangzhou 510632, China

Edited by Chris Whitfield

Zinc is an essential metal in bacteria. One important bacterial zinc transporter is AdcA, and most bacteria possess AdcA homologs that are single-domain small proteins due to better efficiency of protein biogenesis. However, a double-domain AdcA with two zinc-binding sites is significantly overrepresented in *Streptococcus* species, many of which are major human pathogens. Using molecular simulation and experimental validations of AdcA from *Streptococcus pyogenes*, we found here that the two AdcA domains sequentially stabilize the structure upon zinc binding, indicating an organization required for both increased zinc affinity and transfer speed. This structural organization appears to endow *Streptococcus* species with distinct advantages in zinc-depleted environments, which would not be achieved by each single AdcA domain alone. This enhanced zinc transport mechanism sheds light on the significance of the evolution of the AdcA domain fusion, provides new insights into double-domain transporter proteins with two binding sites for the same ion, and indicates a potential target of antimicrobial drugs against pathogenic *Streptococcus* species.

Zinc is an essential trace element for all pathogenic bacteria because many crucial enzymes and transcription factors require zinc to maintain their native structure and biological functionality. It has been shown that zinc homeostasis is essential to invasion and infection by pathogenic bacteria (1, 2). Zinc directly binds to metalloenzymes or zinc finger proteins and functions as a structural or catalytic element to regulate cellular metabolism and gene expression. It also has an immune function as an anti-inflammatory agent (3, 4). To colonize in different organs, pathogenic bacteria must adapt to changing metal concentrations in various host microenvironments (5). In general and at high concentrations, zinc has been shown to be toxic (6). However, the free zinc concentration in host tissues is usually very low, ~1 μM in lung alveolar lavages for example (7, 8). Therefore, pathogenic bacteria require an efficient zinc import system for survival, especially in hosts.

Most bacteria have evolved several zinc uptake systems to strictly control zinc concentration within cells, such as ZnuABC in *Escherichia coli*, the Zur family (YcdH/YceA/YcdI) *in Bacillus subtilis*, and AdcABC in *Streptococcus pyogenes* and *Streptococcus pneumoniae* (9–11). The ABC system in bacteria is usually composed of a zinc-binding lipoprotein, a membrane permease, and an ATPase. In Gram-positive bacteria, the lipoprotein (*e.g.* AdcA from *S. pyogenes*) attached to the cell surface acquires zinc from the environment and interacts with the membrane permease to deliver the zinc ions into the cell via ATPase, which provides energy (12).

S. pyogenes is one of the most pathogenic bacteria, causing infectious diseases that can be lethal (13, 14). It must adapt to a wide range of metal concentrations in host microenvironments during the colonization process (1, 15). Two membrane-associated lipoproteins, AdcA and Lbp, have been identified as essential zinc uptake systems as the deletion of these two genes resulted in a requirement for zinc and decreased infectivity in a mouse model. Both proteins belong to the metal-binding receptor family as ABC transporters. Most bacterial zinc-uptake proteins contain only one zinc-binding domain. Indeed, the protein Lbp in *S. pyogenes* and its homologous protein AdcAII in *S. pneumoniae* are single-domain, zinc-binding proteins whose structures and functions have been intensively investigated (16–18).

In contrast, AdcA in *S. pyogenes* is yet not crystallized and characterized. AdcA proteins in *S. pneumoniae* and *S. pyogenes* share 61% homology, and both are predicted to have two zinc-binding domains. *In vitro* studies indicated higher zinc affinity for the N-terminal domain. The *S. pyogenes* AdcA double-domain organization is rare among other bacterial genera. Due to the distinct translation and mRNA degradation mechanisms, bacteria synthesize large proteins in a much less efficient manner than do eukaryotes (19). Therefore, bacteria tend to maintain proteins as small as possible. Thus, there should be a dis-

This work was supported by National Natural Science Foundation of China Grants 21571082 (to X. S.) and 21271086 (to Q.-Y. H.), National High-Tech Research and Development Program (863) of China Grant 2014AA020504 (to G. Z.), Guangdong Natural Science Research Grants 2015A030313334 (to X. S.) and 32213027/32215077 (to Q.-Y. H.), and Guangzhou Science and Technology Grant 201607010228 (to X. S.). The authors declare that they have no conflicts of interest with the contents of this article.

This article contains Figs. S1–S8, Tables S1 and S2, and structures constructed using homology modeling.

[1] These authors contributed equally to this work.
[2] To whom correspondence may be addressed. Tel. and Fax: 86-20-85227039; E-mail: tqyhe@email.jnu.edu.cn.
[3] To whom correspondence may be addressed. Tel.: 86-20-85224031; E-mail: zhanggong@qq.com.
[4] To whom correspondence may be addressed. Tel. and Fax: 86-20-85226165; E-mail: tsunxs@jnu.edu.cn.

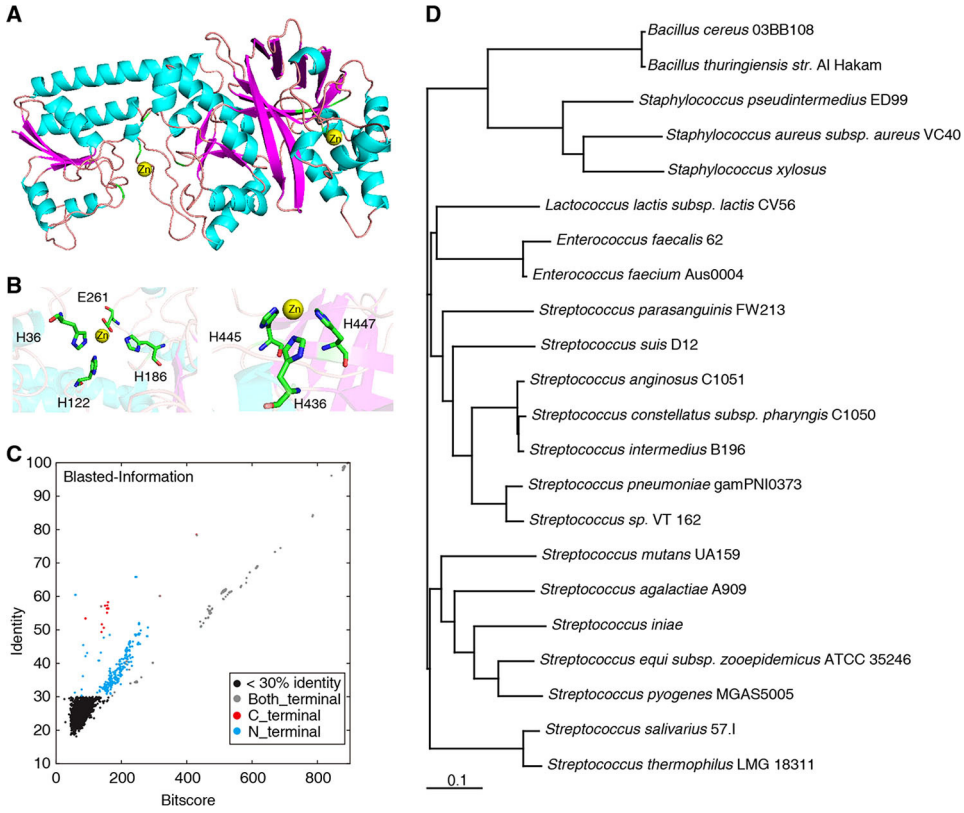

Figure 1. Structure and phylogeny of AdcA. *A*, the three-dimensional structure of *S. pyogenes* AdcA, constructed using homology modeling. Two zinc ions are indicated as *yellow balls*. *B*, the zinc-binding residues in the N- and C-terminal domains of AdcA. *C*, homology search with AdcA of 3,449 bacterial genomes using Blastx. Each *dot* represents the best match within each bacterial genome. *Black dots*, <30% homology; *red dots*, single-domain proteins homologous to the C-terminal domain of AdcA; *blue dots*, single-domain proteins homologous to the N-terminal domain of AdcA; *gray dots*, double-domain proteins homologous to the entire AdcA. *D*, phylogenetic tree of the bacterial species with double-domain AdcA homologs.

tinct functional and beneficial role for the double-domain AdcA for zinc uptake in *Streptococcus* species.

In this study, we applied molecular modeling and molecular dynamics simulation to assess the dynamic structure and functional features of the two domains of *Streptococcus* AdcA. Based on the computational results, we propose a sequential structural stabilization model for the two fused domains that can conduct an interdomain conformational change when bound to zinc, an exceptional feature that enhances zinc uptake efficiency in zinc-deficient environments as compared with single-domains proteins. We further experimentally validated the predicted features and the double-domain organization that endows *Streptococcus* with unique survival advantages in zinc-depleted environments.

Results

Double-domain AdcA homologs are conserved and overrepresented in Streptococcus

We first constructed the *S. pyogenes* AdcA structure using homology modeling, taking as templates the most homologous crystal structures of *B. subtilis* Bsu-YcdH (43.9% sequence identity to the N-terminal domain; Protein Data Bank code 2O1E) and *E. coli* San-YodA (47.3% sequence identity to the C-terminal domain, Protein Data Bank code 1TXL) (Fig. S1B). The constructed AdcA structure contains the amino acid residues 31–515 (Fig. 1*A*), which is almost full-length except for the predicted signal peptide (amino acids 1–30; Fig. S1A). The modeled structure gained a discrete optimized potential energy score of −49,727.9, indicating that this structure was approximately at the optimal low-energy state (20). A Ramachandran plot indicated that the modeled three-dimensional structure was reasonable (Fig. S1C). Virtual docking analysis suggested a zinc-binding center in the N-terminal domain (His-36, His-122, His-186, and Glu-261) and a zinc-binding center in the C-terminal domain (His-436, His-445, and His-447) (Fig. 1*B*). The two predicted zinc-binding sites, located in the highly conserved area, were in conformity with the principle of ConSurf evolutionary conservation patterns (21–23).

To determine the universality of the double-domain organization of AdcA homologs in bacteria, we compared *S. pyogenes* AdcA against 3,449 completely sequenced bacterial genome sequences in the NCBI database using the Blastx tool. We found 649 proteins with more than 30% homology to AdcA. Among these, 31 proteins were single-domain zinc-binding proteins homologous to the C-terminal domain, 408 proteins contained a single zinc-binding domain homologous to the N-terminal domain, and 210 were double-domain proteins (Fig. 1*C*). These 210 double-domain proteins belonged to 22 species, 14 of which belonged to *Streptococcus*, showing a significant overrepresentation of this genus ($p = 4.3608 \times 10^{-159}$ by Fisher exact test). A phylogenic tree constructed based on these species showed that the 14 *Streptococcus* species evolved in two branches and that the evolutionary dis-

tances were maintained below 0.22, indicating that these double-domain zinc-binding proteins were highly conserved in *Streptococcus* during evolution from the common ancestor as compared with the other species (Fig. 1*D*). These structural results implied that *Streptococcus* AdcA possesses a unique ability for zinc uptake.

The N-terminal domain stabilizes the protein structure more strongly than does the C-terminal domain upon zinc binding

To predict the properties of *S. pyogenes* AdcA, we performed molecular dynamics (MD)[5] simulations on the homology model. Independent replications of the MD simulation using random initial atomic velocities resulted in similar trajectories. All trajectories reached equilibrated conformation within 5 ns. These timescales are 1–2 orders of magnitude shorter than the timescale for forming any secondary structure. To exclude the formation of new secondary structures, we further performed 300-ns MD simulations for apo-AdcA and Zn_2-AdcA, a timescale that is sufficient to represent the conformational change of complex proteins (24, 25). Compared with the initial state, there was no obvious change in conformation or hydrogen bonds in the equilibrium state (Fig. S5, A–C). Moreover, the trend of change in secondary structures, caused by binding of the two zinc ions, in MD simulations was consistent with CD spectrum experimental results (Fig. 2*C* and Table S2). The merged results from the initial structure and the average structure of the equilibrium state are shown in Fig. S5D. These show that the simulated structure is close to its native state in physiological solutions.

Next, we simulated AdcA structures without zinc atoms (apo-AdcA), with zinc in the N-terminal binding center (Zn-N-AdcA) alone, with zinc in the C-terminal binding center (Zn-C-AdcA) alone, and with zinc in both binding centers (Zn_2-AdcA) (Fig. 2*A*). Trajectories of 40-ns MD simulations revealed the highest root mean square displacement (RMSD) for apo-AdcA, indicating that zinc binding stabilizes the protein structure (Fig. 2*B*). Indeed, Zn_2-AdcA had the lowest RMSD, indicating that it has the highest rigidity among all four forms. This was confirmed by CD spectra (Fig. 2*C*): the unordered fraction of AdcA was reduced from 19.1 ± 0.14 (apo-AdcA) to 11.2 ± 0.56% (Zn_2-AdcA) when saturated by zinc, and the helix fraction slightly increased from 53.2 ± 0.62 to 58.8 ± 0.14% (Table S2).

However, the structural rigidity of the two zinc-binding centers deviated remarkably. We calculated the root mean square fluctuation (RMSF) of the zinc-binding residues; a lower RMSF indicates higher rigidity. The four residues of the N-terminal domain (His-36, His-122, His-186, and Glu-261) showed reduced RMSF values after binding zinc, whereas two of the three residues in the C-terminal domain (His-436, His-445, and His-447) showed increased RMSF values (Fig. 2*D*) (24). These results indicated that zinc stabilizes only the N-terminal domain and that flexibility of the C-terminal domain is not affected by zinc. This was echoed by the RMSF of all C-α atoms of the two domains (Fig. 2*E*): 132 of 291 residues (45.5%) in the N-terminal domain showed reduced RMSF after binding zinc, whereas 45 of 194 residues (23.9%) in the C-terminal domain showed reduced RMSF after binding zinc.

Moreover, the radius of gyration (R_g) within the period of equilibrium also suggested a more flexible structure of Zn-C-AdcA, Zn-N-AdcA, and Zn_2-AdcA compared with apo-AdcA (Fig. 2, *F* and *G*). To further analyze the R_g values between these three curves, we used symbolic aggregate approximation to evaluate the statistical differences in detail (Fig. S6). The major goal of the symbolic aggregate approximation algorithm is to convert time-series data to a symbolic representation, *e.g.* a < b < c < d. Then, the mean value of each section is calculated (26). This method can be used to accurately distinguish differences in the data (27, 28). The strings, converted from the R_g values of Zn-C-AdcA, Zn-N-AdcA, and Zn_2-AdcA, were shown as dcbbcbcb, cbacbabc, and cbaabaab, respectively (Fig. S6). Thus, the R_g of Zn-C-AdcA was considerably greater than that of Zn-N-AdcA, and Zn-N-AdcA had a similar R_g compared with Zn_2-AdcA (Fig. 2, *F* and *G*, and Fig. S6). Therefore, we posit that the N-terminal domain stabilizes the protein structure more than does the C-terminal domain and possesses a higher affinity for zinc. Interestingly, zinc binding in one domain influenced rigidity in the other domain. Zinc binding to the N-terminal domain (Zn-N-AdcA) reduced the RMSF of 18.7% of the residues in the C-terminal domain, and Zn-C-AdcA reduced the RMSF of 12.4% of the residues in the N-terminal domain (Fig. 2*E*). This suggested that the two domains, each with distinct zinc-binding properties, may synergize upon zinc binding, creating new conformational features that do not exist in the single domains.

Affinity and speed: New features emerge by synergy of the two domains

To validate the above mentioned postulations, we mutated key binding residues to alanine to abolish the N-terminal (H36A/H122A/H186A/E261A) or C-terminal (H436A/H445A/H447A) zinc-binding sites while maintaining the full lengths of N-AdcA and C-AdcA. To completely remove the interactions between the two domains, we created an N-lobe (residues 31–321) and a C-lobe (residues 322–515) to mimic the single-domain AdcA that exists in most bacterial species (Fig. 3*A*). These mutants and the WT AdcA were expressed and purified (Fig. S3, A and B). The inductively coupled plasma MS measurement showed that all the purified proteins did not contain any metal ions.

To detect the strength differences of the two binding domains of AdcA, a 4-(2-pyridylazo)resorcinol (PAR) competition test with Zn_2-AdcA was performed. As shown in Fig. 3*B*, PAR could only capture one zinc from Zn_2-AdcA under normal conditions, whereas it could capture other zinc atoms only under harsh denaturation conditions, *e.g.* 6 M guanidine hydrochloride. These results of the competition test showed that the differences in zinc binding strength of the N- and C-terminal domains are significant.

[5] The abbreviations used are: MD, molecular dynamics; PAR, 4-(2-pyridylazo)resorcinol; TPEN, *N*,*N*,*N*′,*N*′-tetrakis(2-pyridylmethyl)ethylenediamine; RMSF, root mean square fluctuation; RMSD, root mean square displacement; R_g, radius of gyration; ITC, isothermal titration calorimetry; SASA, solvent-accessible surface area.

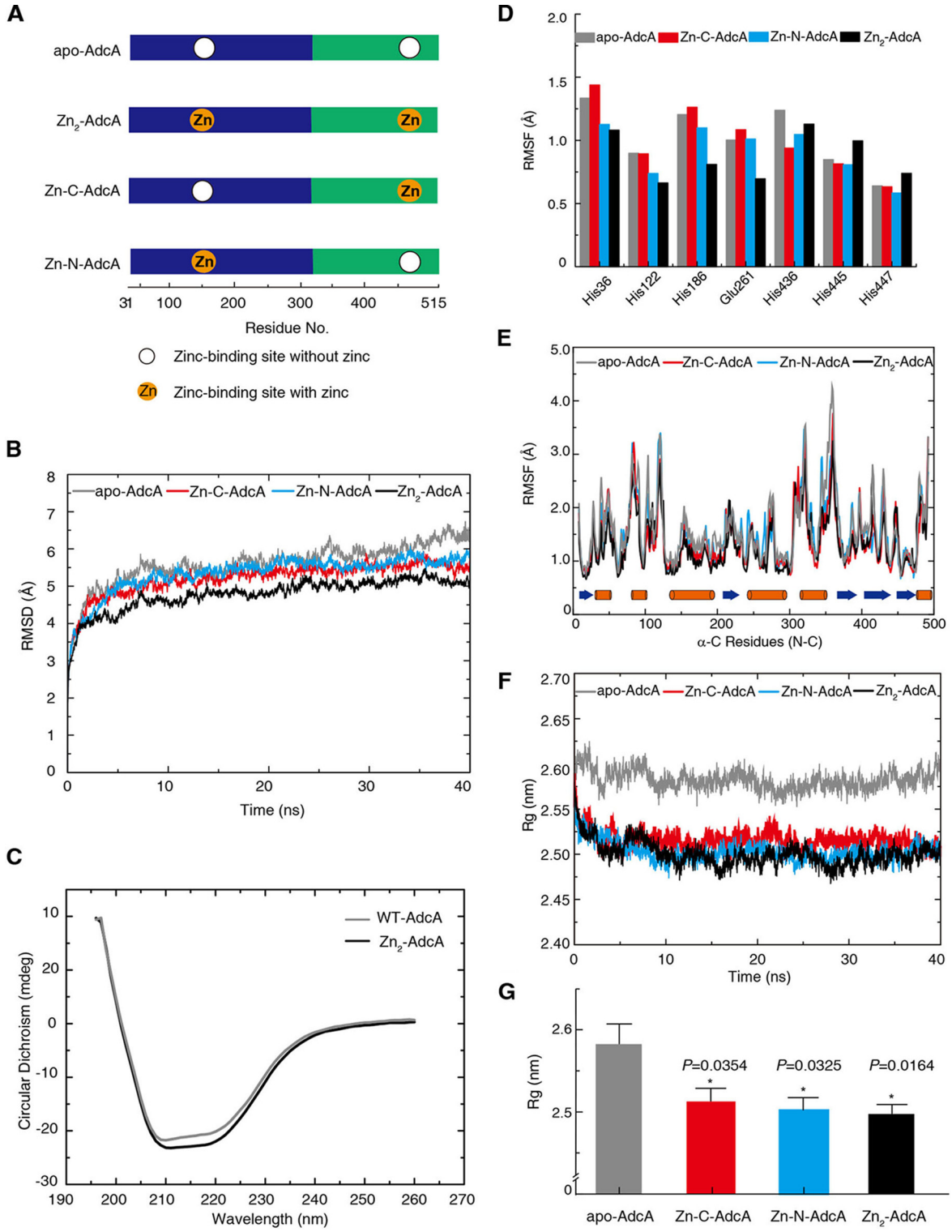

Figure 2. Protein flexibility. *A*, the four protein model constructs used in the molecular dynamic simulations. *B*, the time evolution of the average RMSD of the C-α atoms in the apo-AdcA (*gray*), Zn-C-AdcA (*red*), Zn-N-AdcA (*bright blue*), and Zn_2-AdcA (*black*) simulations. Each sample was repetitively analyzed three times (40-ns duration). *C*, secondary structures of AdcAs with or without zinc ions determined by CD spectrometry. *D*, the RMSF of the C-α profile of residues in the two active binding sites of apo- and zinc-bound AdcA MD trajectories. *E*, the RMSF of C-α for all residues calculated over the 40-ns trajectory in the absence and presence of zinc. *Orange* and *blue bars* denote α-helices and β-strands, respectively. *F*, time evolution of the C-α average of the R_g values. *G*, corresponding *p* value statistics of R_g shown in *F*, and *error bars* represent S.D.

We further experimentally determined the zinc-binding affinities of WT and mutant AdcA using isothermal titration calorimetry (ITC), and the calculated values of *N*, K_D, ΔH, and ΔS are shown in Fig. 3, *C–G*. The K_D of the WT AdcA for Zn^{2+} was measured as 27 ± 7.3 nM, much lower than that of any mutant (Fig. 3*C*). The independently expressed N-lobe and C-lobe had K_D values of 93 ± 8.2 nM and 2.6 ± 0.3 μM, respectively (Fig. 3, *F* and *G*), confirming that the N-lobe has higher

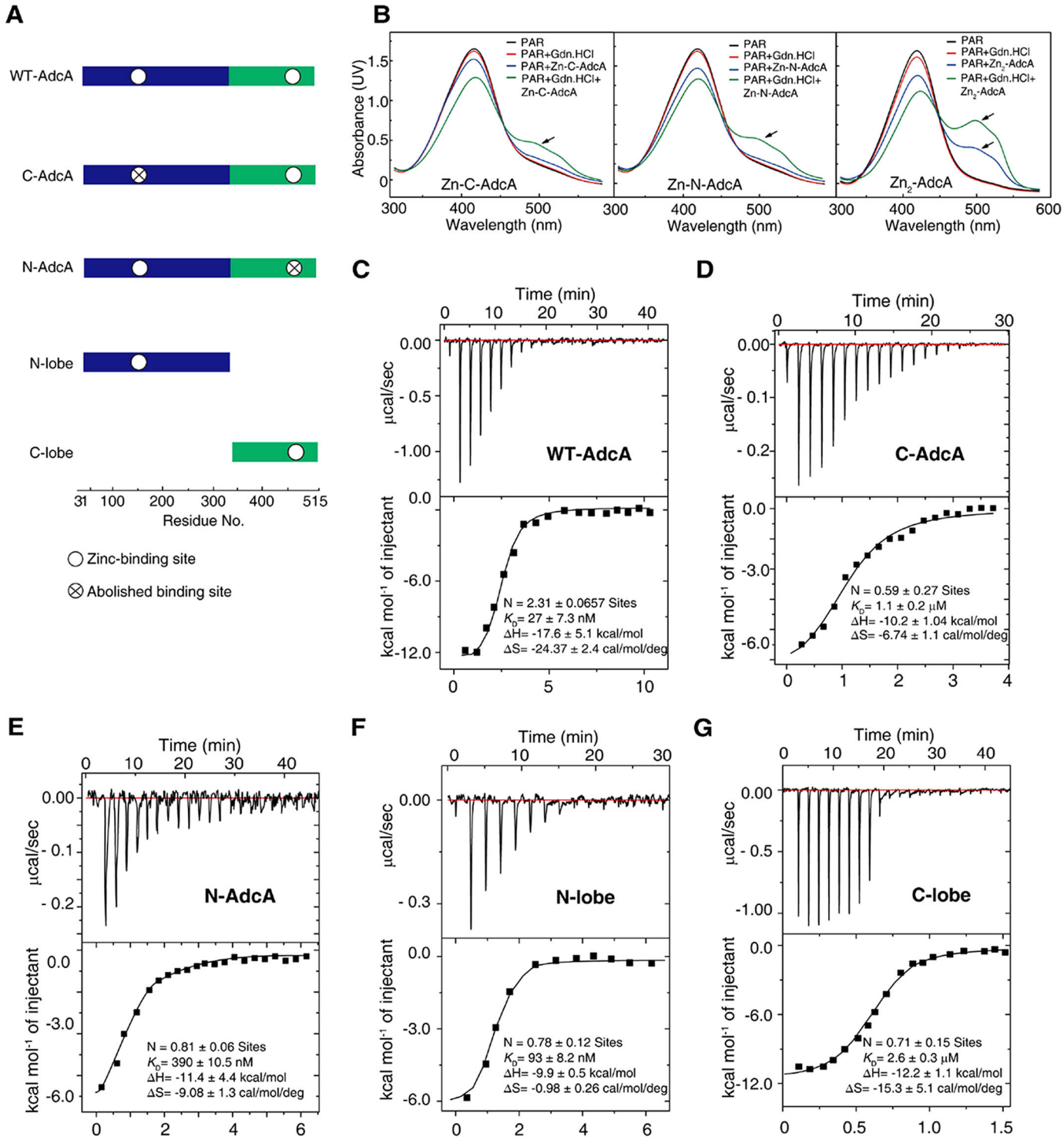

Figure 3. Zinc-binding affinity of AdcAs and PAR competition for zinc ions. *A*, the five protein constructs used to determine the biophysical properties. The constructs were overexpressed in *E. coli* BL21 (DE3) strain and purified. *B*, UV-visible spectra of PAR, which competes for zinc, for Zn-C-AdcA, Zn-N-AdcA, and Zn_2-AdcA in the presence or absence of guanidine hydrochloride (*Gdn.HCl*). *C–G*, isothermal titration calorimetry binding curves of WT AdcA (*C*), C-AdcA (*D*), N-AdcA (*E*), the N-lobe (*F*), and the C-lobe (*G*) at 25 °C. The parameters *N*, K_D, ΔH, and ΔS are shown in the diagrams.

zinc-binding affinity than does the C-lobe. Moreover, the full-length expressed mutants N-AdcA and C-AdcA had dissociation constants of 390 ± 10.5 nM and 1.1 ± 0.2 μM (Fig. 3, *D* and *E*). Notably, the independently expressed N-lobe had a stronger binding affinity for Zn^{2+} than did full-length N-AdcA, implying that the two domains interact with each other, influence each other's conformation, and thus regulate zinc affinity. Thermodynamic data on enthalpy changes (ΔH) and entropy changes ($T\Delta S$) of AdcAs were detected by ITC. For zinc binding, WT AdcA, C-AdcA, N-AdcA, the N-lobe, and the C-lobe were, respectively, found to have ΔH values of −17.6 ± 5.1, −10.2 ± 1.04, −11.4 ± 4.4, −9.9 ± 0.5, and −12.2 ± 1.1 kcal/mol and

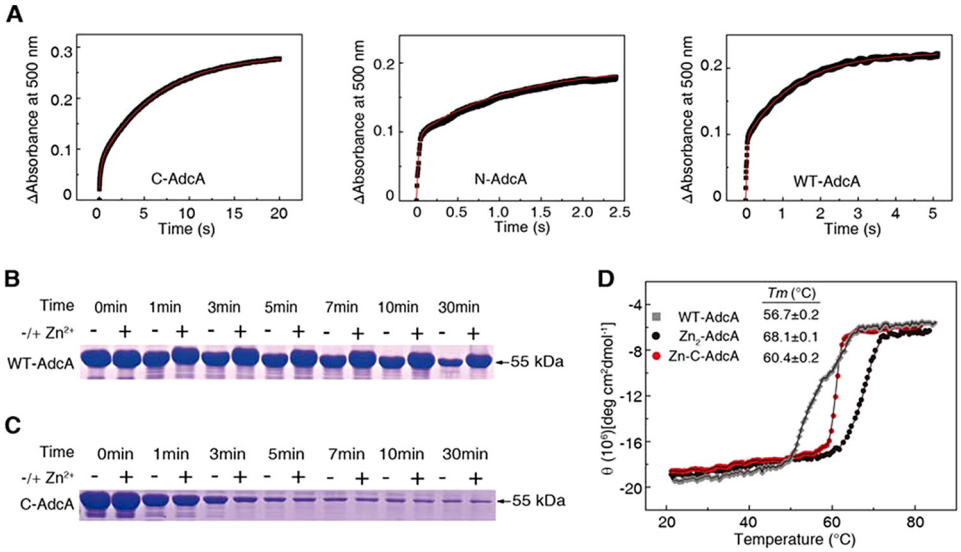

Figure 4. Biochemical, thermodynamic, and kinetic characterization to verify protein stability. *A*, kinetics of AdcA binding to zinc. Time-dependent reactions were created using 10 μM apo-form proteins mixed with 40 μM $Zn(PAR)_2$. *B*, proteinase K sensitivity of WT AdcA. Proteins (15 μg) were subjected to proteinase K (30 μg/liter) for 0, 1, 3, 5, 7, 10, and 30 min. *C*, proteinase K sensitivity of C-AdcA. *D*, thermal stabilities of WT AdcA, Zn_2-AdcA, and Zn-C-AdcA. Thermal unfolding transitions were monitored using far-UV CD spectra at 223 nm. *deg*, degrees.

$T\Delta S$ values of -7.3 ± 0.7, -2.0 ± 0.3, -2.7 ± 0.4, -0.3 ± 0.07, and -4.5 ± 1.5 kcal/mol. The values of ΔH and $T\Delta S$ indicated that zinc binding to the five models of AdcA is both enthalpically and entropically favorable with ΔH being the main driving factor.

Next, we measured the zinc binding kinetics of AdcA. As expected, N-AdcA, with higher affinity-bound zinc, had very fast kinetics and a two-component reaction ($k_1 = 45.45 \pm 0.07$ s^{-1} and $k_2 = 0.93 \pm 0.02$ s^{-1}, $A_1 = 0.099 \pm 0.000$ and $A_2 = 0.161 \pm 0.002$). In contrast, C-AdcA, with a less rigid structure, bound zinc at a much lower rate and had a second-order reaction. The fast reaction was a minor reaction with an amplitude of $A_1 = 0.154 \pm 0.026$ and $k_1 = 5.02 \pm 0.03$ s^{-1}, whereas the major reaction had the kinetic parameters $A_2 = 0.271 \pm 0.036$ and $k_2 = 0.15 \pm 0.01$ s^{-1} (Fig. 4*A*). WT AdcA, with two binding centers, revealed a similarly fast process ($k_1 = 41.05 \pm 0.01$ s^{-1}) as compared with N-AdcA and a much-accelerated slow process ($k_2 = 0.75 \pm 0.02$ s^{-1}) as compared with C-AdcA (Fig. 4*A*). This indicated that, in the presence of a low concentration of zinc, the N-terminal domain rapidly bound a zinc atom and stabilized the entire protein structure. The C-terminal domain was then stabilized to obtain a faster binding speed. Both the zinc binding velocity and affinity constant of the C-terminal domain are 1 order of magnitude slower and weaker, respectively, than that of the N-terminal domain.

To validate the structural stability of the zinc-bound N-terminal domain, we performed proteinase K digestion assays. Zinc-saturated AdcA was almost intact after 30 min of proteinase K digestion, whereas the apo form of AdcA was mostly digested (Fig. 4*B*). In contrast, C-AdcA was vulnerable to proteinase K attack in both the apo and zinc-bound forms (Fig. 4*C*) due to the lack of stabilization by the zinc-bound N-terminal domain. This was echoed by the melting temperature of these two proteins. The melting temperature of Zn-C-AdcA was similar to that of WT AdcA and much lower than that of Zn_2-AdcA (Fig. 4*D*). These results suggested that the zinc in the N-terminal domain was crucial for enhancing the zinc binding rate in the C-terminal domain. As the C-terminal domain binds zinc with less affinity, it can pass zinc downstream to other zinc-binding proteins that finally transport zinc into the cell.

Structural alteration upon zinc binding

To investigate in detail the structural alterations after zinc binding, we compared the MD simulation trajectories of apo-AdcA, Zn-N-AdcA, and Zn_2-AdcA. The mean distance matrix showed remarkably decreased interdomain distances when the N-terminal domain bound a zinc atom (29) (Fig. 5*A*), which can be visualized in the steady-state three-dimensional conformations (Fig. 5*B* and Fig. S4). This can be explained by N-terminal domain stabilization of the C-terminal domain via interatomic interactions of the peptide chains. The mean distance matrix of Zn-N-AdcA showed adjacency of the residue pairs Asn-237 and Lys-460, Glu-235 and Lys-457, Ser-258 and Asp-453, Lys-280 and Asp-453, Lys-280 and Tyr-430, and Asp-273 and Lys-421. All these interactions are interdomain interactions (30, 31) spanning the entire interaction surface between the two domains (Fig. 5*C*).

Moreover, the interdomain surface is linked by at least 10 hydrogen bonds (Fig. 5*C*, *red dashed lines*). This multianchored stabilization mechanism explains the stability of the induced conformational change. The induced conformation dramatically decreased the distance among the residues around the zinc-binding pocket of the C-terminal domain (32), specifically Lys-300 and Glu-481, Glu-299 and Tyr-360, and Lys-354 and Lys-409 (Fig. 5, *D* and *E*), facilitating the binding to zinc. This explained the increased affinity of the C-terminal domain when the N-terminal domain was zinc-bound. In summary, these analyses demonstrated the structural basis of the synergy between the two domains for both metal-binding affinity and rate.

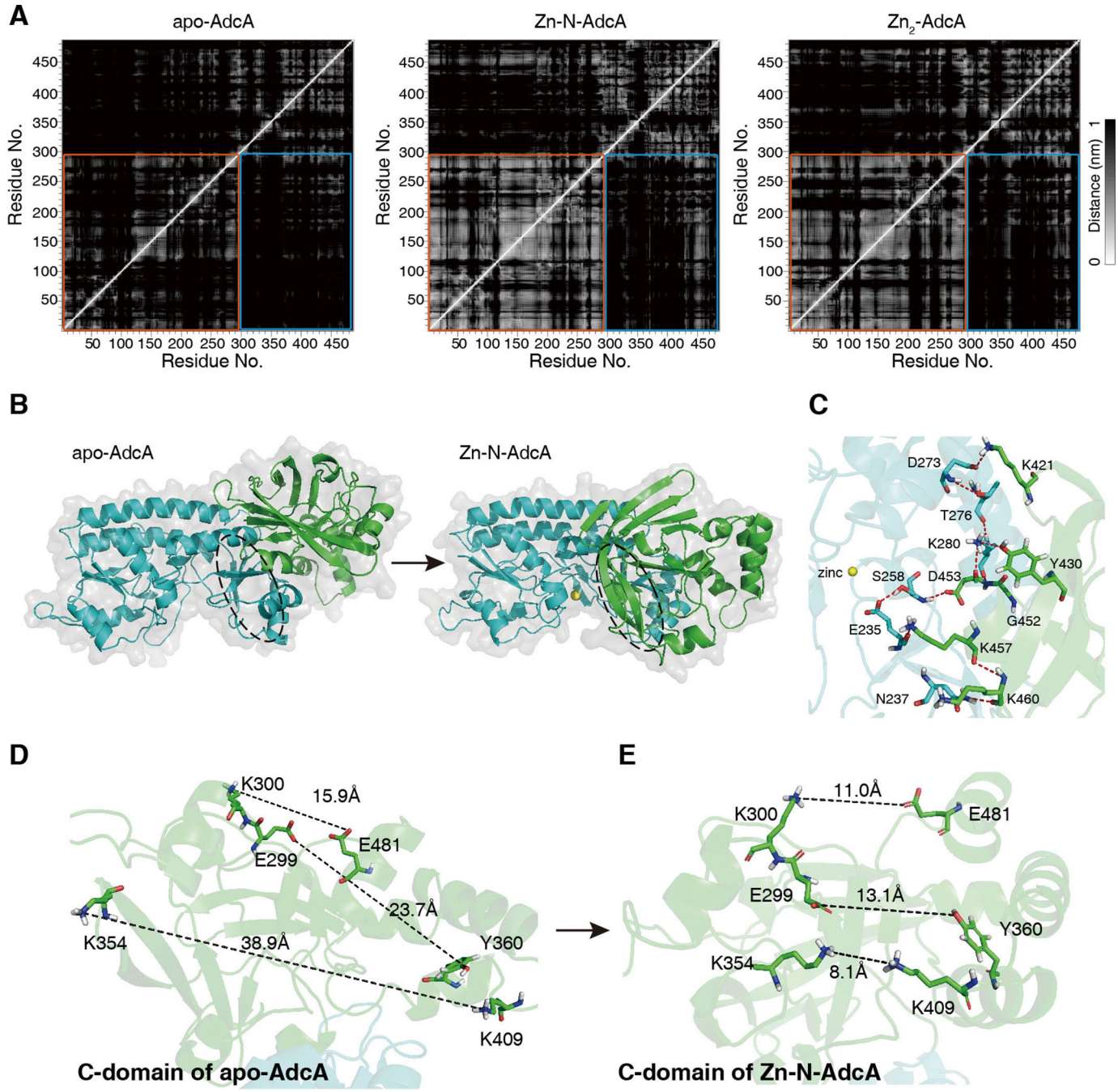

Figure 5. Zinc binding in the N-terminal domain of AdcA stabilizes the C-terminal domain conformation for C-terminal zinc binding. *A*, mean distance matrices for the different states of the proteins are shown for apo-AdcA, Zn-N-AdcA, and Zn_2-AdcA. *Lighter colors* represent closer distances between two amino acid residues. An *orange box* denotes the N-terminal domain, and the *bright blue boxes* denote the interdomain distances. *B*, representative structures of apo-AdcA and Zn-N-AdcA. *C*, hydrogen bonds (*red dashes*) on the N- and C-terminal interaction surfaces. *D* and *E*, the differences in the C-terminal domain conformations were compared between apo-AdcA and Zn-N-AdcA, and the distances between the selected residues were measured.

Verification of the interaction surface of the N-terminal and C-terminal domains using MD simulations

We showed that the interface interactions rely on 10 hydrogen bonds between the N-terminal and C-terminal domains, involving the 12 amino acid residues depicted in Fig. 5*C*. To evaluate the contributions of the 12 residues to the interface interaction, we successively established 12 single-site mutants of Zn-N-AdcA. However, we found that none of the single-site mutants caused any reduction of the surface formation (Fig. S7). Subsequently, we established four Zn-N-AdcA mutants, mutating groups of the abovementioned residues according to their vicinity: D273A, T276A, and K421A; K280A, S258A, Y430A, D453A, and G452A; E235A, N237A, K460A, and K457A; and a variant mutated for all 12 residues. In the fully mutated protein, only one zinc ion was located in the N-terminal domain of AdcA.

The trajectory analyses of the 100-ns MD simulations showed that these mutant proteins took a much longer time (~20 ns; Fig. 6*A*) to reach the equilibrium state than did the WT Zn-N-AdcA (~5 ns; Fig. 2*B*). Especially the fully mutated pro-

tein did not even reach the equilibrium state in 100 ns (Fig. 6*A*). The result revealed that the 12 residues of the interaction surface are crucial to stabilizing the skeleton of the whole protein. Among the 12 residues, the six residues at positions 273, 276, 280, 430, 452, and 453 showed increased RMSF values after mutation to alanine (Fig. 6*B*).

We next assessed whether the hydrogen bonds stabilized the interaction surface, measuring the solvent-accessible surface area (SASA) where a smaller SASA value represents tighter structures. The mutant structures showed that abolishing any group of hydrogen bonds reduced the interaction surface (Fig. 6, *C–E*). Abolishing all hydrogen bonds completely destroyed the interaction surface. These results were also reflected in the SASA values (Fig. 6*G*).

To further investigate the role of these hydrogen bonds in the allosteric cross-talk between the two domains, we calculated the average separation distance between representative residue pairs around the zinc-binding pocket of the C-terminal domain (Fig. 6, *C–F*), specifically Lys-300 and Glu-481, Glu-299 and Tyr-360, and Lys-354 and Lys-409. The three corresponding average separation distances for each of the above mentioned mutants were 15.8, 28.8, and 10.6 Å (Fig. 6*C*, D273A, T276A, and K421A); 12.5, 20.4, and 22.1 Å (Fig. 6*D*, K280A, S258A, Y430A, D453A, and G452A); 8.7, 20.9, and 10.9 Å (Fig. 6*E*, E235A, N237A, K460A, and K457A); 21.5 Å, 22.3 Å, and 24.6 Å (Fig. 6*F*, fully mutated variant). Significantly, conformational changes in the C-terminal domain induced by the N-terminal domain of these four mutant proteins were reduced to varying extents when compared with WT Zn-N-AdcA (11.0, 13.1, and 8.1 Å; Fig. 5*E*). Among these, the fully mutated variant had the greatest impact on the conformation of the C-terminal domain. Based on these results, we propose a possible mechanism: the N-terminal domain firmly and rapidly binds a zinc ion and draws the C-terminal domain closer, relying on hydrogen bonds. Subsequently, this stabilizes the C-terminal domain and tightens the zinc-binding pocket, which facilitates zinc binding, especially in zinc-depleted environments.

A synergistic double-domain AdcA endows growth advantages at low zinc concentrations

The double-domain AdcA increased both affinity and rate of zinc binding. Therefore, we postulate that bacteria use the synergistic organization of the double-domain AdcA to more efficiently take up zinc, even under conditions of extremely low environmental zinc concentrations, to maintain growth. Due to the lack of genetic manipulation tools in *S. pyogenes*, we performed experiments in *S. pneumoniae*. We used *N*,*N*,*N*′,*N*′-tetrakis(2-pyridylmethyl)ethylenediamine (TPEN) to chelate zinc ions in the media and to create a zinc-deficient environment. With increasing TPEN concentrations, significant growth hindrance was observed from 20 μM TPEN (Fig. 7*A*) where the free zinc concentration was estimated to be ~150–300 nM. Then we used this concentration to test zinc uptake ability. The deletion strain Δ*adcA* Δ*adcAII* of *S. pneumoniae*, with a deleted zinc transporter AdcA system, grew significantly slower than the WT strain and stopped growing at an A_{600} of 0.22. Expression of either N-AdcA or C-AdcA in the deletion strain did not rescue growth, whereas expression of the double-domain AdcA almost completely rescued the growth to a rate similar to that of the WT strain (Fig. 7*B*). This result validated that the double-domain organization facilitated bacterial growth in a zinc-deficient environment.

Discussion

Generally, bacterial genomes tend to encode smaller proteins (267 amino acids long on average) than do eukaryotes (33). Major reasons include that mRNA is degraded by endonucleases in bacteria, making it difficult to translate full-length long proteins (19), and multidomain large proteins need proper translational pausing sites for correct folding, which may be disturbed by environmental and molecular factors (34–36). Indeed, in most bacterial species, the homologs of *Streptococcus* AdcA are single-domain small proteins. Therefore, the evolution of the double-domain AdcA in *Streptococcus* (515 amino acids) should be unlikely unless an emergent feature benefits the adaptive survival of *Streptococcus* in host environments, such as lung tissue (1–2 μM zinc) (7). A previous study suggested that N-terminal domains in two-domain proteins are biased to be shorter and are predicted to fold faster than their C-terminal counterparts (37). However, AdcA is a special case of an overall trend in two-domain proteins as its N-terminal domain is longer than its C-terminal domain.

In this study, we found that double-domain AdcA with two zinc-binding sites is significantly overrepresented in *Streptococcus* species by homology comparison between AdcA and the library of known genomes of bacteria. We have shown evidence that fusion of the two domains creates a new, emergent, structure-based functional advantage that is greater than the sum of the advantages provided by two independent domains. In the presence of zinc, the N-terminal domain firmly and quickly binds a zinc ion and changes its conformation. This conformation change in the N-terminal domain subsequently stabilizes the C-terminal domain and tightens its zinc-binding pocket, facilitating zinc binding, especially in zinc-depleted environments. The relatively less stable conformation and weak binding of the C-terminal domain ensure a rapid transfer of zinc to the downstream transporter, the transmembrane protein AdcB of *Streptococcus* species (Fig. 8). Otherwise, overly stable and strong binding would limit the cyclic utilization of zinc transporters on the cell surface and the flux of zinc into the cell as shown in Fig. 7*B*. This interdomain synergy via interatomic interaction of the peptide chains endows *Streptococcus* with exceptional zinc uptake efficiency in zinc-depleted media, thus benefiting its survival in harsh conditions, *e.g.* in lung alveolar lavages with low zinc concentration (7). Therefore, the emergent features of the fused domains could be a simple evolutionary response to specific metal-deficient conditions (Fig. 8).

As organisms need multiple trace elements for physiology, other metal ion transporters are also found to exist in double-domain formats with two binding sites for the same ion. Examples are not restricted to bacteria and include the human transferrin receptor that binds two samarium ions (Protein Data Bank code 1CX8), human copper-lactoferrin that binds two copper ions (Protein Data Bank code 1LFI), *Rapana thomasiana* hemocyanin that binds two copper ions (Protein Data Bank code 1LNL), lactoferrin that binds two Fe^{3+} ions (Protein Data

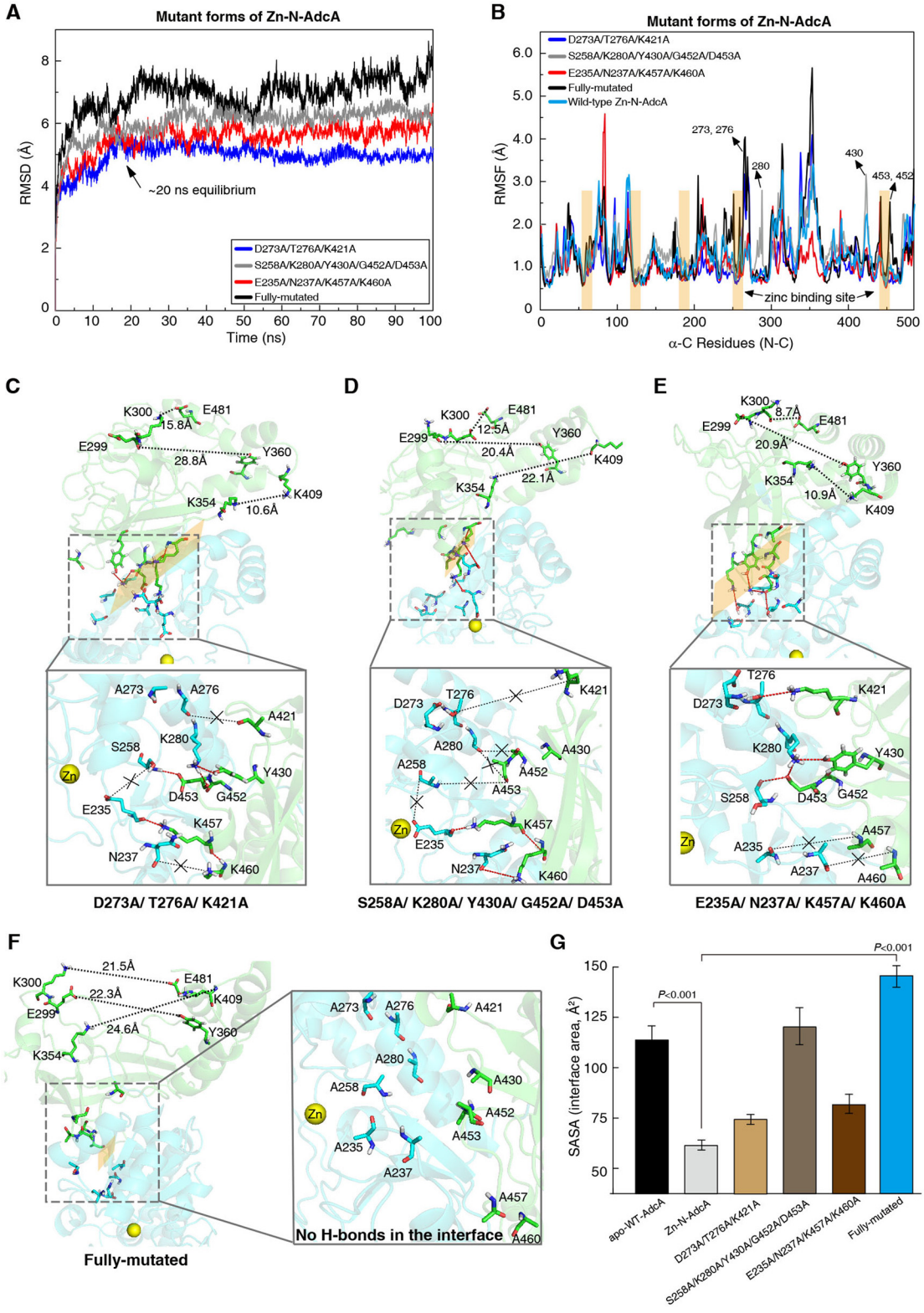

Figure 6. Identification of the N- and C-terminal interaction surfaces of Fig. 5C. *A*, the time evolution of RMSD values in the four mutant Zn-N-AdcAs, D273A/T276A/K421A (*blue*), S258A/K280A/Y430A/G452A/D453A (*gray*), E235A/N237A/K457A/K460A (*red*), and the fully mutated variant (*black*). *B*, the RMSF of the C-α for all residues of the four mutant proteins calculated over the 100-ns trajectory. The RMSF values of the mutated amino acids became greater. Hydrogen bonds (*red dashes*), missing hydrogen bonds (*black dashes with* "×"), interaction surfaces (*dotted line frame*), and conformation changes of the C-terminal domain are shown in the four mutated forms of Zn-N-AdcA, D273A/T276A/K421A (*C*), S258A/K280A/Y430A/G452A/D453A (*D*), E235A/N237A/K457A/K460A (*E*), and the fully mutated variant (*F*). *G*, the calculated SASA values of the interface area, respectively, and *error bars* represent S.D.

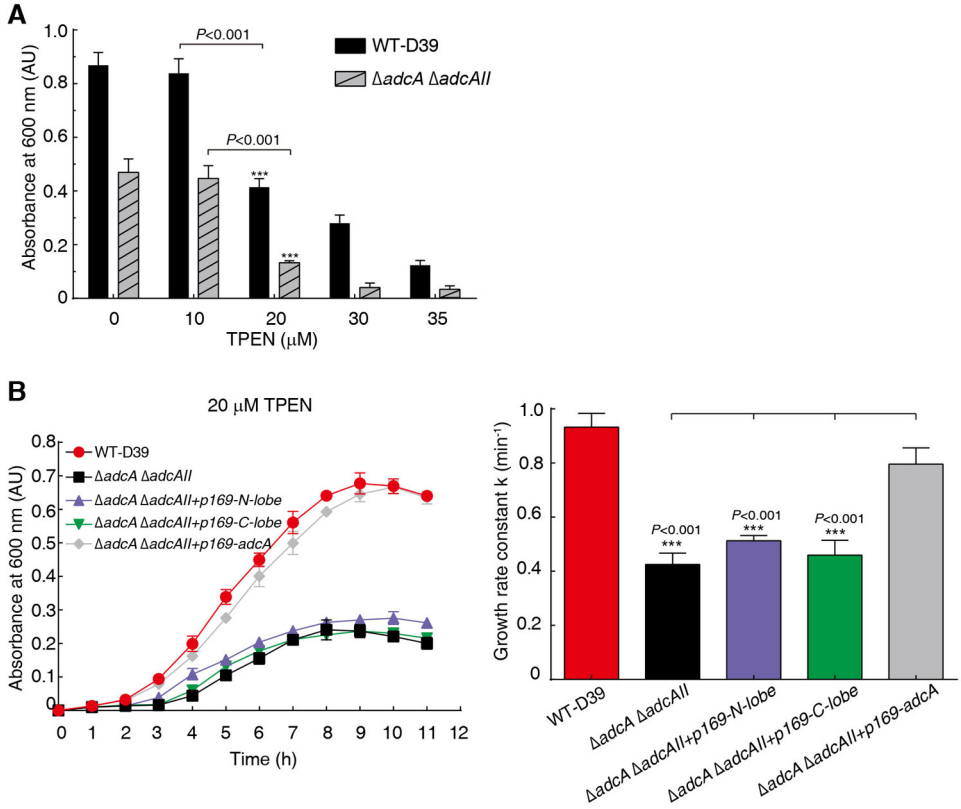

Figure 7. The growth of bacteria in a zinc-deficient environment. *A*, the absorbance at 600 nm of WT *S. pneumoniae* (D39) and Δ*adcA* Δ*adcAII* mutant strains cultured in C+Y medium containing TPEN at different final concentrations for 8 h. *B*, the growth curves (*left*) of D39 strains grown in C+Y medium containing 20 μM TPEN and corresponding growth rate constants (*right*) calculated for WT, Δ*adcA* Δ*adcAII*, and Δ*adcA* Δ*adcAII* with the N-lobe, C-lobe, and full-length *adcA*, respectively, and *error bars* represent S.D. *AU*, absorbance units.

Bank code 1B7Z), and others. Our model for emergent interdomain synergy may provide new insights to better understand such cases.

Our finding also emphasizes the interdomain conformation change after metal binding, which may implicate a novel target for antimicrobial drugs against pathogenic *Streptococcus* species. No AdcA homolog was found in the human genome using the HMMER tool (Fig. S8), suggesting that such a conformation may not exist in the human proteome. Therefore, a rationally designed blocker molecule that binds the interdomain surfaces may abolish the synergy of the two domains, sufficiently reduce the influx of zinc, and inhibit the growth of the pathogen. The action mechanism of the designed blocker molecule would be totally different from that of existing antibiotics. To be noted, the interdomain interaction is stabilized by as many as 10 hydrogen bonds (38, 39), suggesting that mutation of a few amino acids will not abolish the interaction, thus minimizing the probability of the bacteria to evolve resistance by simple point mutations. This finding may help during the treatment of bacterial infections caused by *Streptococcus*.

In conclusion, we suggest a special zinc transportation mechanism mediated by AdcA in *Streptococcus* species. An N-terminal binding site preferentially binds a zinc ion and induces stabilization of the overall conformation of the protein via interdomain interaction. This allows the C-terminal binding domain to acquire a zinc ion while also allowing zinc bound by the C-terminal domain to be more likely and preferentially released (Fig. 8). This model elucidates the significance of the evolution of the domain fusion, provides new insights on double-domain transporter proteins with two binding sites for the same ion, and implicates a novel target for antimicrobial drugs against pathogenic *Streptococcus* species.

Experimental procedures

MD simulation

The preprocessed structures of apo-AdcA, Zn-N-AdcA (mutation of the three zinc-binding ligands in the C-terminal domain), Zn-C-AdcA (mutation of the four binding ligands in the N-terminal domain), and Zn_2-AdcA, obtained from homology modeling, were used as starting conformations. These conformations were solvated in cubic periodic boxes containing 0.15 M Na^+ and Cl^- ions to neutralize the system (40, 41). No zinc ions were added to the simulated solution, representing a zinc-deficient environment. Energy minimization in each AdcA system was performed for the first relaxed energy through 400 steps of the steepest descent energy method and then continued with 25,000 steps of the conjugate gradient method. All MD simulations were simulated at a temperature of 310.15 K (42) and pressure of 1 atm (43) by the Gromacs 4.6.6 package with the simple point charge (SPC) model for liquid water as described previously (44). The zinc ion force field of the Gromacs package has been developed in various aspects (45), including bonds, angles, impropers, metal center, dihedrals, and normal van der Waals, and it is suitable for the protein-zinc simulation (46–48). Therefore, we used the default

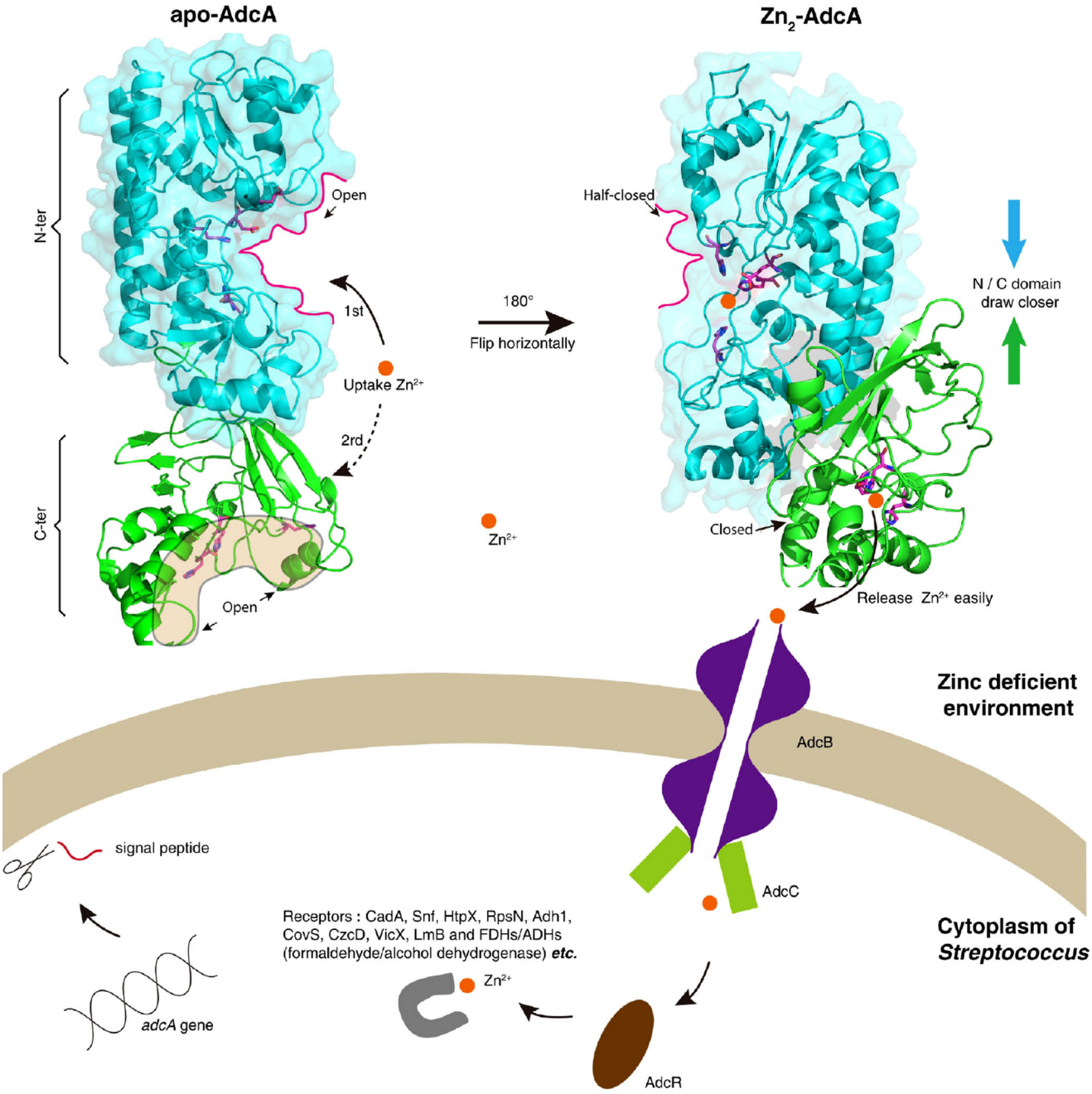

Figure 8. The model of zinc uptake in *Streptococcus* via AdcA from a zinc-deficient environment. The N-terminal (*N-ter*) domain and the C-terminal (*C-ter*) domain of AdcA are colored *cyan* and *green*, respectively. The two binding sites are represented as an open state in apo-AdcA but a half-closed or closed state in Zn_2-AdcA. Compared with the C-terminal domain, the N-terminal domain has a faster binding rate and stronger affinity for zinc ions. The release of a zinc ion from the C-terminal domain of AdcA to AdcB is easier than that from the N-terminal domain. The receptor proteins for zinc ions in the *Streptococcus* cytoplasm are represented schematically by the *gray loop*.

parameters of Gromos43a1 force field for the simulation of AdcAs with zinc. We set the value of the emtol convergence criterion at 1,000 kJ/mol/nm, and the temperature in the box was determined by the v-rescale temperature coupling method. We used the particle mesh Ewald method to calculate electrostatic interactions within the system. The position restraint simulations for the systems were executed for 50 ps, and then we actualized the 40-ns unrestrained simulation.

We simulated four structures of the AdcA system as mentioned above, and each system was repetitively carried out three times with random initial velocities (49). To avoid equilibration artifacts, we calculated the structural features using trajectory data ranging from 10 to 40 ns, which represents the structures at their equilibrated states. To validate the equilibrium of each structure, we also performed 300-ns MD simulations for apo-AdcA and Zn_2-AdcA. We analyzed RMSD, RMSF, secondary structure, and R_g using Gromacs tools g_rms, g_rmsf, do_dssp, and g_gyrate, respectively. The mean distances between residues were calculated by the Gromacs tool g_dist. Protein structures were visualized using PyMOL 1.7. The matrix of residue distance fluctuations was represented by methods described previously (50, 51), and it can be used to describe the plasticity

and elasticity of residues in structural fluctuations. To reduce the deviation, all MD trajectories data were derived from three replicates (Fig. S2).

Homology modeling

The NCBI BLAST search tool was used to find several proteins that have the highest homology to AdcA. Then a multiple sequence alignment and cluster analysis were performed using proteins with high scores through the software package ClustalX 2.0. The tertiary structure of AdcA was modeled using MODELLER in Accelrys Discovery Studio Client 4.1 (52, 53). Proteins San-YodA (Protein Data Bank code 1TXL) and Bsu-YcdH (Protein Data Bank code 2O1E), with a high level of amino acid sequence homology to AdcA, were selected as the templates to model the initial stage of the three-dimensional structure of AdcA. Subsequently, flexible molecule docking between AdcA and zinc was processed via the LigandFit module of the software to find the lowest energy conformation combining the ligand and the receptor in the active site (Fig. S1B). The reliability of the model was evaluated by discrete optimized potential energy and Ramachandran plots (54).

Construction, expression, and purification of WT AdcA

Genomic DNA extracted from *S. pyogenes* MGAS5005 (ATCC BAA-947^{TM}) was used as a template to amplify the *adcA* gene (1,488 bp without the N-terminal signal). PCR primers were designed to introduce the restriction enzyme sites of BamHI and SalI for the *adcA* gene (Table S1). Detailed methods were described previously (55). Purified AdcA protein was confirmed using 12% SDS-PAGE and identified using MS (ABI 4800 MALDI-TOF/TOF) according to a method described previously (56) (Fig. S3D).

Proteinase K resistance experiments

To test the proteinase K (Roche Diagnostics) sensitivity of AdcA, the same amounts of apo-, zinc-saturated WT, and mutant AdcA (15 μg) were incubated with 30 μg/liter proteinase K in 20 mM Tris-HCl buffer (pH 8.0) containing $CaCl_2$ (10 mM) at 25 °C for 0, 1, 3, 5, 7, 10, and 30 min. Proteolysis was stopped by addition of 5 μl of 100 mM phenylmethanesulfonylfluoride and boiling for 10 min. Digestion fragments were analyzed by 12% SDS-PAGE. Gels were stained with Coomassie Blue R-250 and scanned with Image Scanner II (GE Healthcare).

Circular dichroism spectroscopy

Far-UV CD studies were performed with a CD spectrometer (Chirascan, Applied Photophysics Ltd., Leatherhead, UK) using a quartz cuvette with a 0.1-cm optical path length at a wavelength range of 260–190 nm at room temperature. CD data were collected for 5 μM apo-, zinc-saturated WT, and mutant AdcA in 20 mM Tris-HCl (pH 7.4) in a data pitch of 1 nm at a scanning rate of 100 nm/min. Each CD spectrum was repeated three times, and a blank containing the same buffer was subtracted as a reference. Analysis of the experimental data was performed using the software CDPro. CD spectra were also used to study the thermal stability of proteins in the absence or presence of zinc ions. Thermal unfolding curves were monitored from 20 to 90 °C using an increase rate of 2 °C/min by detecting the loss of secondary structures at 222 nm. Each data set was obtained three times using steps of 0.5 °C, and T_m values were calculated by the included Glob3 software.

Growth media and growth curve assays

Casein-based semisynthetic liquid culture medium (C+Y medium) was used to culture WT and mutant D39 strains (57). To establish Zn(II) starvation conditions, TPEN (Sigma-Aldrich) was added into C+Y medium at final concentrations of 10, 20, 30, and 35 μM (8, 58, 59). We determined the growth curves for WT and Δ*adcA* Δ*adcAII* double-mutant strains cultured in zinc starvation medium at 37 °C with 5% CO_2 for 12 h by measuring A_{600} values at different time points. For the double-mutant strain, 20 μM TPEN significantly inhibited bacterial growth at an A_{600} of ~0.15 after 12 h of culture. We selected 20 μM TPEN to add to the medium to create zinc deficiency. Different treated *S. pneumoniae* strains were inoculated into C+Y medium, and growth curves were determined three times.

Construction, expression, and purification of mutant AdcAs

Based on the predicted structure of AdcA with molecular docking, the N-terminal binding site is composed of His-36, His-122, His-186, and Glu-261, and the C-terminal binding site is composed of His-436, His-445, and His-447. The four amino acids in the N-terminal domain and the three amino acids in the C-terminal domain were simultaneously mutated to alanine to generate the four-residue mutant H36A/H122A/H186A/E261A (C-AdcA) and the three-residue mutant H436A/H445A/H447A (N-AdcA), respectively, using a QuikChange mutagenesis kit (Stratagene) with the original pGEX-4T-*adcA* plasmid as template. The primers used for constructing the mutants are listed in Table S1. All the constructed plasmids were transformed to *E. coli* XL1-blue, which were then screened on LB agar plates containing 100 μg/ml ampicillin followed by DNA sequencing (Invitrogen). The plasmids with correct sequences were transformed to *E. coli* BL21 (DE3) for expression. Expression and purification of mutant AdcAs were conducted as done for WT AdcA.

Construction of the ΔadcA/ΔadcAII double-mutant strain

The primer sequences used to construct mutant strains are listed in Table S1. The double mutant strain was constructed as described previously (60, 61). Long flanking homology PCR products contained an antibiotic resistance cassette (erythromycin or spectinomycin) flanked by 600-bp-long fragments homologous to the end of each target gene, *adcA* or *adcAII*. Then the long flanking homology PCR fragments were transformed into *S. pneumoniae* D39 competent cells. Transformants were selected with antibiotic-containing Columbia sheep blood agar plates after overnight culture at 37 °C with 5% CO_2 and confirmed by DNA sequence analysis and PCR (Fig. S3C). The mutant strain was stable after six sequential passages in Todd-Hewitt broth with 0.5% yeast extract (THY) medium in the absence of antibiotics.

Construction of the three types of overexpression strains

To construct overexpression strains of *S. pneumoniae* D39 for recovery of expression of different types of AdcA, the plas-

mid pIB169 (p169) was used in this study (62). We constructed three recombinant plasmids, p169-*N-lobe* (expressing the N-lobe alone), p169-*C-lobe* (expressing the C-lobe alone), and p169-*adcA* (expressing full-length adcA) (Fig. S3C). The constructed plasmids were transformed into the Δ*adcA* Δ*adcAII* double mutant strain, and the positive clones were screened using Columbia blood plates with 4 μg/ml chloramphenicol. The transformants with the recovered genes were verified by PCR. All primers are listed in Table S1.

Comparison of the zinc binding strength of the two domains of AdcA

To compare the binding strength of the N-terminal and C-terminal domains of AdcA, a special zinc metallochromic indicator, PAR, was used. A final concentration of 100 μM PAR was added to 5 μM Zn-N-AdcA, Zn-C-AdcA, and Zn_2-AdcA in 20 mM Tris-HCl (pH 7.4) with or without 6 M guanidine hydrochloride. UV/visible absorbance spectra were obtained from 300 to 600 nm after a 5-min equilibration at room temperature.

Zinc-binding affinity determination

To determine the binding affinities of WT and mutant AdcAs with zinc, ITC experiments were performed at 25 °C using a MicroCalorimeter Auto-ITC 200 (Malvern, UK). Prior to the experiments, the instrument was washed with deionized water, and the $ZnCl_2$ and AdcAs were dissolved in the same solution buffer (20 mM Tris-HCl, 100 mM NaCl (pH 7.4)) (55). Typically, an experiment consisted of loading the syringe with zinc ions at a concentration at least 10-fold higher than the AdcAs samples, which were placed in the cell. The titration parameters were set as follows: 2 μl of $ZnCl_2$ solution were injected into the 300-μl protein sample cell during each titration with 15–20 injections. The delay time between injections was set at 200 s to ensure thermal equilibrium before the next injection. The background heat effect was subtracted by addition of zinc alone to the buffer. All integrated heat data were analyzed using Origin 7.0 software for fitting calculations.

Stopped-flow absorbance kinetics

Stopped-flow spectroscopy was performed on a stopped-flow reaction analyzer (Chirascan SF.3, Applied Photophysics Ltd.) using the absorbance mode to monitor absorbance changes at 495 nm over time. The $Zn(PAR)_2$ complex (200 μM PAR in 20 mM Tris-HCl buffer combined with 40 μM Zn^{2+}) was loaded into the A drive syringe, the B drive syringe was filled with 10 μM apo-AdcAs, and transient mixing of the reaction was driven by bottled nitrogen. Experimental parameters were set as follows: 1-nm bandwidth, 10-mm optical path, 495 nm scanned wavelength with a 475-nm filter, and a 25 °C water bath temperature. Buffer incubated with $Zn(PAR)_2$ was used as the reference. Tests were repeated until consistent results were obtained. The collected data were analyzed using exponential equations.

Author contributions—X. S., G. Z., and Q.-Y. H. conceived and designed the project. K. C., C. W., N. L., J. H., and B. Z. performed the experiments and data analysis. X. C. analyzed data. K. C., N. L., X. S., and G. Z. wrote the manuscript.

Acknowledgment—We are grateful for the high-performance platform of Jinan University.

References

1. Zalewski, P. D., Truong-Tran, A. Q., Grosser, D., Jayaram, L., Murgia, C., and Ruffin, R. E. (2005) Zinc metabolism in airway epithelium and airway inflammation: basic mechanisms and clinical targets. A review. *Pharmacol. Ther.* **105,** 127–149 CrossRef Medline
2. Murakami, M., and Hirano, T. (2008) Intracellular zinc homeostasis and zinc signaling. *Cancer Sci.* **99,** 1515–1522 CrossRef Medline
3. Zhou, X., Cooper, K. L., Sun, X., Liu, K. J., and Hudson, L. G. (2015) Selective sensitization of zinc finger protein oxidation by reactive oxygen species through arsenic binding. *J. Biol. Chem.* **290,** 18361–18369 CrossRef Medline
4. Prasad, A. S. (2014) Zinc: an antioxidant and anti-inflammatory agent: role of zinc in degenerative disorders of aging. *J. Trace Elem. Med. Biol.* **28,** 364–371 CrossRef Medline
5. Ma, L., Terwilliger, A., and Maresso, A. W. (2015) Iron and zinc exploitation during bacterial pathogenesis. *Metallomics* **7,** 1541–1554 CrossRef Medline
6. Djoko, K. Y., Ong, C. L., Walker, M. J., and McEwan, A. G. (2015) The role of copper and zinc toxicity in innate immune defense against bacterial pathogens. *J. Biol. Chem.* **290,** 18954–18961 CrossRef Medline
7. Shafeeq, S., Kuipers, O. P., and Kloosterman, T. G. (2013) The role of zinc in the interplay between pathogenic streptococci and their hosts. *Mol. Microbiol.* **88,** 1047–1057 CrossRef Medline
8. Tedde, V., Rosini, R., and Galeotti, C. L. (2016) Zn^{2+} uptake in *Streptococcus pyogenes*: Characterization of *adcA* and *lmb* null mutants. *PLoS One* **11,** e0152835 CrossRef Medline
9. Gaballa, A., and Helmann, J. D. (1998) Identification of a zinc-specific metalloregulatory protein, Zur, controlling zinc transport operons in *Bacillus subtilis*. *J. Bacteriol.* **180,** 5815–5821 Medline
10. Patzer, S. I., and Hantke, K. (2000) The zinc-responsive regulator Zur and its control of the *znu* gene cluster encoding the ZnuABC zinc uptake system in *Escherichia coli*. *J. Biol. Chem.* **275,** 24321–24332 CrossRef Medline
11. Capdevila, D. A., Wang, J., and Giedroc, D. P. (2016) Bacterial strategies to maintain zinc metallostasis at the host-pathogen interface. *J. Biol. Chem.* **291,** 20858–20868 CrossRef Medline
12. Blindauer, C. A. (2015) Advances in the molecular understanding of biological zinc transport. *Chem. Commun.* **51,** 4544–4563 CrossRefMedline
13. Bessen, D. E. (2009) Population biology of the human restricted pathogen, *Streptococcus pyogenes*. *Infect. Genet. Evol.* **9,** 581–593 CrossRef Medline
14. Cunningham, M. W. (2000) Pathogenesis of group A streptococcal infections. *Clin. Microbiol. Rev.* **13,** 470–511 CrossRef Medline
15. Magneson, G. R., Puvathingal, J. M., and Ray, W. J., Jr. (1987) The concentrations of free Mg^{2+} and free Zn^{2+} in equine blood plasma. *J. Biol. Chem.* **262,** 11140–11148 Medline
16. Lawrence, M. C., Pilling, P. A., Epa, V. C., Berry, A. M., Ogunniyi, A. D., and Paton, J. C. (1998) The crystal structure of pneumococcal surface antigen PsaA reveals a metal-binding site and a novel structure for a putative ABC-type binding protein. *Structure* **6,** 1553–1561 CrossRef Medline
17. McDevitt, C. A., Ogunniyi, A. D., Valkov, E., Lawrence, M. C., Kobe, B., McEwan, A. G., and Paton, J. C. (2011) A molecular mechanism for bacterial susceptibility to zinc. *PLoS Pathog.* **7,** e1002357 CrossRef Medline
18. Loisel, E., Jacquamet, L., Serre, L., Bauvois, C., Ferrer, J. L., Vernet, T., Di Guilmi, A. M., and Durmort, C. (2008) AdcAII, a new pneumococcal Zn-binding protein homologous with ABC transporters: biochemical and structural analysis. *J. Mol. Biol.* **381,** 594–606 CrossRef Medline
19. Valleriani, A., Zhang, G., Nagar, A., Ignatova, Z., and Lipowsky, R. (2011) Length-dependent translation of messenger RNA by ribosomes. *Phys. Rev. E Stat. Nonlin. Soft Matter Phys.* **83,** 042903 CrossRef Medline
20. Unissa, A. N., Sudha, S., Selvakumar, N., and Hassan, S. (2011) Binding of activated isoniazid with acetyl-CoA carboxylase from *Mycobacterium tuberculosis*. *Bioinformation* **7,** 107–111 CrossRef Medline

21. Armon, A., Graur, D., and Ben-Tal, N. (2001) ConSurf: an algorithmic tool for the identification of functional regions in proteins by surface mapping of phylogenetic information. *J. Mol. Biol.* **307,** 447–463 CrossRef Medline
22. Glaser, F., Pupko, T., Paz, I., Bell, R. E., Bechor-Shental, D., Martz, E., and Ben-Tal, N. (2003) ConSurf: identification of functional regions in proteins by surface-mapping of phylogenetic information. *Bioinformatics* **19,** 163–164 CrossRef Medline
23. Ashkenazy, H., Abadi, S., Martz, E., Chay, O., Mayrose, I., Pupko, T., and Ben-Tal, N. (2016) ConSurf 2016: an improved methodology to estimate and visualize evolutionary conservation in macromolecules. *Nucleic Acids Res.* **44,** W344–W350 CrossRef Medline
24. Skjaerven, L., Grant, B., Muga, A., Teigen, K., McCammon, J. A., Reuter, N., and Martinez, A. (2011) Conformational sampling and nucleotide-dependent transitions of the GroEL subunit probed by unbiased molecular dynamics simulations. *PLoS Comput. Biol.* **7,** e1002004 CrossRef Medline
25. Miettinen, M. S., Knecht, V., Monticelli, L., and Ignatova, Z. (2012) Assessing polyglutamine conformation in the nucleating event by molecular dynamics simulations. *J. Phys. Chem. B* **116,** 10259–10265 CrossRef Medline
26. Keogh, E., and Lin, J. (2005) Clustering of time-series subsequences is meaningless: implications for previous and future research. *Knowl. Inf. Syst.* **8,** 154–177 CrossRef
27. Junejo, I. N., and Aghbari, Z. A. (2012) Using SAX representation for human action recognition. *J. Vis. Commun. Image Represent.* **23,** 853–861 CrossRef
28. Georgoulas, G., Karvelis, P., Loutas, T., and Styliosa, D. C. (2015) Rolling element bearings diagnostics using the Symbolic Aggregate approXimation. *Mech. Syst. Signal Process.* **60–61**, 220–242 CrossRef
29. He, Y., Maisuradze, G. G., Yin, Y., Kachlishvili, K., Rackovsky, S., and Scheraga, H. A. (2017) Sequence-, structure-, and dynamics-based comparisons of structurally homologous CheY-like proteins. *Proc. Natl. Acad. Sci. U.S.A.* **114,** 1578–1583 CrossRef Medline
30. Rose, A. S., Elgeti, M., Zachariae, U., Grubmüller, H., Hofmann, K. P., Scheerer, P., and Hildebrand, P. W. (2014) Position of transmembrane helix 6 determines receptor G protein coupling specificity. *J. Am. Chem. Soc.* **136,** 11244–11247 CrossRef Medline
31. Czub, J., Wieczór, M., Prokopowicz, B., and Grubmüller, H. (2017) Mechanochemical energy transduction during the main rotary step in the synthesis cycle of F1-ATPase. *J. Am. Chem. Soc.* **139,** 4025–4034 CrossRef Medline
32. Timmins, A., Saint-André, M., and de Visser, S. P. (2017) Understanding how prolyl-4-hydroxylase structure steers a ferryl oxidant toward scission of a strong C-H bond. *J. Am. Chem. Soc.* **139,** 9855–9866 CrossRef Medline
33. Brocchieri, L., and Karlin, S. (2005) Protein length in eukaryotic and prokaryotic proteomes. *Nucleic Acids Res.* **33,** 3390–3400 CrossRef Medline
34. Zhang, G., Hubalewska, M., and Ignatova, Z. (2009) Transient ribosomal attenuation coordinates protein synthesis and co-translational folding. *Nat. Struct. Mol. Biol.* **16,** 274–280 CrossRef Medline
35. Zhang, G., and Ignatova, Z. (2009) Generic algorithm to predict the speed of translational elongation: implications for protein biogenesis. *PLoS One* **4,** e5036 CrossRef Medline
36. Guo, J., Lian, X., Zhong, J., Wang, T., and Zhang, G. (2015) Length-dependent translation initiation benefits the functional proteome of human cells. *Mol. Biosyst.* **11,** 370–378 CrossRef Medline
37. Jacob, E., Unger, R., and Horovitz, A. (2013) N-terminal domains in two-domain proteins are biased to be shorter and predicted to fold faster than their C-terminal counterparts. *Cell Rep.* **3,** 1051–1056 CrossRef Medline
38. Monecke, T., Haselbach, D., Voß, B., Russek, A., Neumann, P., Thomson, E., Hurt, E., Zachariae, U., Stark, H., Grubmüller, H., Dickmanns, A., and Ficner, R. (2013) Structural basis for cooperativity of CRM1 export complex formation. *Proc. Natl. Acad. Sci. U.S.A.* **110,** 960–965 CrossRef Medline
39. Graen, T., Inhester, L., Clemens, M., Grubmüller, H., and Groenhof, G. (2016) The low barrier hydrogen bond in the photoactive yellow protein: a vacuum artifact absent in the crystal and solution. *J. Am. Chem. Soc.* **138,** 16620–16631 CrossRef Medline
40. Sun, X., Ågren, H., and Tu, Y. (2014) Microsecond molecular dynamics simulations Provide Insight into the Allosteric Mechanism of the Gs Protein Uncoupling from the beta2 adrenergic receptor. *J. Phys. Chem. B* **118,** 14737–14744CrossRef Medline
41. Chen, W., Lou, J., Hsin, J., Schulten, K., Harvey, S. C., and Zhu, C. (2011) Molecular dynamics simulations of forced unbending of integrin $\alpha_v\beta_3$. *PLoS Comput. Biol.* **7,** e1001086 CrossRef Medline
42. Pereira, A. R., Hsin, J., Król, E., Tavares, A. C., Flores, P., Hoiczyk, E., Ng, N., Dajkovic, A., Brun, Y. V., VanNieuwenhze, M. S., Roemer, T., Carballido-Lopez, R., Scheffers, D. J., Huang, K. C., and Pinho, M. G. (2016) FtsZ-dependent elongation of a coccoid bacterium. *MBio* **7,** e00908–e00916 CrossRef Medline
43. Heymann, G., Dai, J., Li, M., Silberberg, S. D., Zhou, H. X., and Swartz, K. J. (2013) Inter- and intrasubunit interactions between transmembrane helices in the open state of P2X receptor channels. *Proc. Natl. Acad. Sci. U.S.A.* **110,** E4045–E4054 CrossRef Medline
44. Kumar, A., and Purohit, R. (2014) Use of long term molecular dynamics simulation in predicting cancer associated SNPs. *PLoS Comput. Biol.* **10,** e1003318 CrossRef Medline
45. Van Gunsteren, F., Eising, B. S. A., Hünenberger, P., Krüger, P., Mark, A., Scott, W., and Tironi, I. (1996) *Biomolecular Simulation: the GROMOS96 Manual and User Guide*, pp. 397–434, Verlag der Fachvereine Hochschulverlag AG an der ETH Zurich, Zurich, Switzerland
46. van Gunsteren, W. F., Daura, X., and Mark, A. E. (2002) GROMOS force field, in *Encyclopedia of Computational Chemistry*, pp. 1211–1216, John Wiley and Sons, New York
47. Manzetti, S., McCulloch, D. R., Herington, A. C., and van der Spoel, D. (2003) Modeling of enzyme-substrate complexes for the metalloproteases MMP-3, ADAM-9 and ADAM-10. *J. Comput. Aided Mol. Des.* **17,** 551–565 CrossRef Medline
48. Park, P. S., Sapra, K. T., Koliński, M., Filipek, S., Palczewski, K., and Muller, D. J. (2007) Stabilizing effect of Zn^{2+} in native bovine rhodopsin. *J. Biol. Chem.* **282,** 11377–11385 CrossRef Medline
49. Li, J., Rossetti, G., Dreyer, J., Raugei, S., Ippoliti, E., Lüscher, B., and Carloni, P. (2014) Molecular simulation-based structural prediction of protein complexes in mass spectrometry: the human insulin dimer. *PLoS Comput. Biol.* **10,** e1003838 CrossRef Medline
50. Morra, G., Potestio, R., Micheletti, C., and Colombo, G. (2012) Corresponding functional dynamics across the Hsp90 Chaperone family: insights from a multiscale analysis of MD simulations. *PLoS Comput. Biol.* **8,** e1002433 CrossRef Medline
51. Best, R. B., Hummer, G., and Eaton, W. A. (2013) Native contacts determine protein folding mechanisms in atomistic simulations. *Proc. Natl. Acad. Sci. U.S.A.* **110,** 17874–17879 CrossRef Medline
52. Li, B. J., Wang, H., Gong, T., Chen, J. J., Chen, T. J., Yang, J. L., and Zhu, P. (2017) Improving 10-deacetylbaccatin III-10-β-O-acetyltransferase catalytic fitness for Taxol production. *Nat. Commun.* **8,** 15544 CrossRef Medline
53. Yan, C., Liu, D., Li, L., Wempe, M. F., Guin, S., Khanna, M., Meier, J., Hoffman, B., Owens, C., Wysoczynski, C. L., Nitz, M. D., Knabe, W. E., Ahmed, M., Brautigan, D. L., Paschal, B. M., *et al.* (2014) Discovery and characterization of small molecules that target the GTPase Ral. *Nature* **515,** 443–447 CrossRef Medline
54. Anil, B., Song, B., Tang, Y., and Raleigh, D. P. (2004) Exploiting the right side of the Ramachandran plot: substitution of glycines by D-alanine can significantly increase protein stability. *J. Am. Chem. Soc.* **126,** 13194–13195 CrossRef Medline
55. Zhang, L., Li, N., Cao, K., Yang, X. Y., Zeng, G., Sun, X., and He, Q. Y. (2017) Crucial residue Trp158 of lipoprotein PiaA stabilizes the ferrichrome-PiaA complex in Streptococcus pneumoniae. *J. Inorg. Biochem.* **167,** 150–156 CrossRef Medline
56. Li, H., Li, N., Xu, Q., Xiao, C., Wang, H., Guo, Z., Zhang, J., Sun, X., and He, Q. Y. (2013) Lipoprotein FtsB in Streptococcus pyogenes binds ferrichrome in two steps with residues Tyr137 and Trp204 as critical ligands. *PLoS One* **8,** e65682 CrossRef Medline
57. Lacks, S., and Hotchkiss, R. D. (1960) A study of the genetic material determining an enzyme in *Pneumococcus*. *Biochim. Biophys. Acta* **39,** 508–518 CrossRef Medline

58. Ding, B., and Zhong, Q. (2017) Zinc deficiency: an unexpected trigger for autophagy. *J. Biol. Chem.* **292,** 8531–8532 CrossRef Medline
59. Mayer, L. S., Uciechowski, P., Meyer, S., Schwerdtle, T., Rink, L., and Haase, H. (2014) Differential impact of zinc deficiency on phagocytosis, oxidative burst, and production of pro-inflammatory cytokines by human monocytes. *Metallomics* **6,** 1288–1295 CrossRef Medline
60. Bayle, L., Chimalapati, S., Schoehn, G., Brown, J., Vernet, T., and Durmort, C. (2011) Zinc uptake by *Streptococcus pneumoniae* depends on both AdcA and AdcAII and is essential for normal bacterial morphology and virulence. *Mol. Microbiol.* **82,** 904–916 CrossRef Medline
61. Wach, A. (1996) PCR-synthesis of marker cassettes with long flanking homology regions for gene disruptions in *S. cerevisiae*. *Yeast* **12,** 259–265 CrossRef Medline
62. Biswas, I., Jha, J. K., and Fromm, N. (2008) Shuttle expression plasmids for genetic studies in *Streptococcus mutans*. *Microbiology* **154,** 2275–2282 CrossRef Medline